Optics and Lasers in Engineering 159 (2022) 107219

Contents lists available at ScienceDirect

Optics and Lasers in Engineering

journal homepage: www.elsevier.com/locate/optlaseng

Modeling and verification of astigmatic digital off-axis holography for burning droplet measurement in a flame tube

Lei Wang[a], Yue Zhao[a], Yu Wang[a], Yingchun Wu[a,b,*], Ge Song[c], Tao Liu[c], Xuecheng Wu[a]

[a] State Key Laboratory of Clean Energy Utilization, Zhejiang University, Hangzhou 310027, China
[b] Huzhou Institue of Zhejiang University, Huzhou 313000, China
[c] Aero Engine Corporation of China, Beijing 100089, China

ARTICLE INFO

Keywords:
Astigmatic digital holography
Off-axis
Flame tube
Aberration compensation
ABCD matrix

ABSTRACT

It is difficult to measure fuel droplets in cylindrical combustors under combustion conditions, but of significance, since fuel behavior is related to combustion performance. In this study, digital off-axis holography and corresponding data treating algorithms are applied to quantify irregular spray droplets in combustion field inside a thick silica flame tube. The analytical expression of an off-axis hologram passing through a pipe is derived based on optic matrix theory and Fresnel diffraction transform. The interference fringes and phase distribution show consistency with the experimental results under the same condition. A modified convolution reconstruction method facing off-axis holography is proposed to locate and quantify the particles in a pipe. The theoretical simulation and experimental results indicate that the proposed method can obtain a clear reconstructed droplet. The image field of view does not change with the reconstruction distance. The particle field obtained through this method has distortion due to the refraction of the curved surface, and can be corrected through ABCD transfer matrix. The calibration method and modified results reveal that the overall droplet size error is lower than 1-pixel width, and real x and y locating errors after correction are lower than 1-pixel width. The depth position error is also discussed through experimental validation. The visualization and quantification results of fuel droplets in the real turbulent spray flame in a circular flame tube prove the feasibility of the proposed theoretical analysis and the reconstruction method.

1. Introduction

Multiphase flows in a pipe or circular cavity widely exist in industrial engineering, for instance, liquid-liquid extraction [1], flame tube, pulverized coal pipe line, and small bubbles in micro flow channels during heat exchange process. The measurement of particles in the limited space (e.g. optical engine) helps understand the relevant flow field dynamic process, particle transportation process and optimize the space design, and thus gets attention. Although most of the test windows are designed to be flat in an optical engine or flow channel in laboratory [2,3], which are convenient for optical diagnostics, it is still necessary to detect particles or flow fields through the curved optical surfaces in some scenarios [4,5]. However, the refractive index of the curved window caused the light refraction, and the existence of astigmatism lead to a deviation between the actual process and the optical measurement signal [6]. Therefore, there exists difficulty to get accurate information of particles in the concave container, such as optical engine, flame tube or cylindrical combustor. Several solutions have been proposed in recent decades. One solution is to select a suitable flow channel configuration to match the refractive index of the test fluid [7,8], which is not feasible for gas-phase fluid. Another application is to investigate the geometric distortion correction parameters of the flow field based on light tracing [9], or used calibrator to correct the distortion [10]. Unfortunately, it is cumbersome to use a calibrator plate to correct three-dimensional (3D) information in a concave container.

Digital holography (DH) is a real three-dimensional imaging technique [11]. The frequency of the fringe chirplet reflects the distance between the object and the image plane, and can be implemented with diffraction theory [12,13] or Lorenz–Mie scattering theory. DH has several applications in droplet aerodynamic fragmentations diagnostics or multiphase flow over the past few decades [14]. Among these scenarios, DH may also suffer from distortion or astigmatism in the propagation medium, which would introduce a curvature of the wave fronts. Astigmatism, commonly encountered in industrial scenarios, would let the symmetrical kernel function inapplicable in holographic simulation

* Corresponding author at: State Key Laboratory of Clean Energy Utilization, Zhejiang University, Hangzhou 310027, China.
E-mail address: wuyingchun@zju.edu.cn (Y. Wu).

https://doi.org/10.1016/j.optlaseng.2022.107219
Received 17 May 2022; Received in revised form 17 July 2022; Accepted 5 August 2022
Available online 14 August 2022

and reconstruction process directly, and would let the accurate three-dimensional measuring and imaging process become challenging.

Figuring out the beam propagating process is helpful to correct the astigmatisms and aberrations of particles in the channel flow. Collins [15] proposed a general formula of Rayleigh–Sommerfeld integral with a lens system based on the ABCD transfer matrix in the 1970s. Later on, the analytical solution of Collin's formula was expressed [16], and the ABCD transfer matrix becomes one of the powerful tools in the theoretical analyzing fringe characteristics of DH with astigmatism. Other theories (i.e. extended Generalized Fresnel Transform (GFT) [17] and Fourier Lorenz-Mie theory [18]) are also useful in exploring the analytical solution of the astigmatic DH. Understanding the transfer function of holography through a pipe can help to correct the aberration and astigmatism of the particles.

Modified reconstruction algorithms including the fractional Fourier transform (FrFt) [19,20], modified convolution formulation [21–23], and extended wavelet transformation [24] were proposed and can correct astigmatism. These studies have enabled the successful application of holographic technology in several channel flow conditions, including micro pipe flow, and plano-concave pipe flow [17,25–27], proving the flexibility of digital inline holography (DIH) to particle diagnostics in a pipe. Unfortunately, DIH faces its intrinsic limitation, the conjugate term effect, which reduces the signal-to-ratio of the results. Under combustion conditions, the strong gradient of the refractive index would lead to worse quality of particle image. This limitation can be eliminated through hardware adjustment like digital off-axis holography (DOH). Existing studies [28,29] prove that DOH is able to filter conjugate terms in the frequency spectrum, improve the SNR, and reduce the influence of combustion flames, plasma, and other components which lead to background noise. DOH shows the privilege to DIH in particle diagnostics in complex conditions with a more complex hardware setup. However, the studies and theoretical analysis on DH with astigmatism rarely involve a digital off-axis scene.

The objective of this research is to visualize the burning droplets inside a flame tube. To achieve this goal, the physical model and performance of DOH in thick pipe systems are mainly studied and discussed, since the shape of the flame tube can be treated as a transparent cylinder (pipe) in physical analysis. Firstly, the intensity distribution in the recording plane and the diffracted light produced by an opaque object located in a pipe are analysed, which is a digital inline hologram. Next, the off-axis reference wave is applied to generate off-axis hologram, and the simulation is compared with the experimental result. Thirdly, a method based on angular spectrum algorithm is proposed to calculate the object image. The reconstructed slice does not distort with the z position, which is conducive to focus metric curve (FMC) calculation. Finally, the distortion of the particle field is eliminated through calibration, and both simulation and experiment results are presented and discussed to illustrate the proposed method.

2. Experimental setup

Fig. 1 shows the experimental configuration. The laser used here is Wedge HF-532, with a wavelength of 532 nm and a pulsed duration of about 700 ps under 25 kHz. The laser beam was filtered and collimated by a spatial filter system and thin lens, and then split into object wave and reference wave. The object wave propagated through a pipe with a refractive index n_p of 1.46, and then interferes with a tilted reference wave in the camera target. The outer (R_{po}) and inner (R_{pi}) radius are 56.7 ± 0.5 mm and 53 ± 0.5 mm separately. The imaging system used a high speed camera (Phantom V2512) with a telescope lens, and had an equivalent pixel size of $d_{pix} = 15.2$ μm, with a spatial resolution of 1024×800. The object wave refracted out of the pipe and propagated to the focal plane, while the tilted reference wave was reflected by the beam splitter and then travelled to the focal plane. The camera then recorded the distorted curved fringes through a lens. To simplify the calculation, the propagation process of the object wave after passing through the flame tube in the experiment is equivalent to free space propagation, denoted by z_{o2d}, representing the equivalent distance from the outer surface of pipe to the focal plane of camera in the case of free space propagation, and is 145 mm in this case. The optical system is set to investigate the fuel behavior in a spray combustion field in a silicon circular flame tube. The RP-3 kerosene fuel is jet from an oil cup atomizer, and the air is pressed into the air cavity and then flows out from the two-stage counter radial swirlers. the droplets, ligaments and liquid sheet mix with the shear flow and further break up in downstream, forming a swirl spray field. The details of the spray system can be seen in our previous study [30]. The effect of turbulent flame and the cylindrical window will cause astigmatism. The optical model of the experimental setup will be proposed in the next section to enable clear burning fuel droplets visualizations through the cylindrical windows.

3. Theoretical analysis

3.1. Digital off-axis hologram formation through a pipe using ABCD matrix

For the generality of the analysis, the flame tube is treated as a pipe, and Fig. 2 is a schematic view of light propagation process of off-axis holography through a pipe according to experimental setup based on ABCD matrices formalism. The collimated Gaussian beam incident on the tube surface can be treated as a circular Gaussian beam, with expression $G_0(x_0, y_0) = \exp\left[-\left(\frac{x_0^2}{\omega_{x0}^2} + \frac{y_0^2}{\omega_{y0}^2}\right)\right]$, and the wave radius $\omega_{x0} = \omega_{y0}$. According to the Collins formula [15], and under the assumption of Fresnel approximation, The laser beam propagates to the particle plane, and the complex amplitude can be expressed as

$$G_1(u,v) = \frac{\exp\left(i\frac{2\pi}{\lambda}G_0\right)}{i\lambda\sqrt{B^x_{l2p}B^y_{l2p}}}\int_{\mathbb{R}^2} G_0(x_0,y_0)\exp\left[i\frac{\pi}{\lambda B^x_{l2p}}\left(A^x_{l2p}x_0^2 - 2ux_0 + D^x_{l2p}u^2\right)\right] \times \exp\left[i\frac{\pi}{\lambda B^y_{l2p}}\left(A^y_{l2p}y_0^2 - 2y_0v + D^y_{l2p}v^2\right)\right]\mathrm{d}x_0\mathrm{d}y_0, \tag{1}$$

where the $A^{x,y}_{l2p}$, $C^{x,y}_{l2p}$, $D^{x,y}_{l2p}$ are elements of the transfer matrix $\mathbf{M}^{x,y}_{l2p}$ from laser to particle plane. It can be found that the beam is distorted to an elliptical beam because the matrix values are different in both x and y direction considering the pipe geometry. The complex field distribution of beam propagating to the focal plane, denoted U_{inine} , can be calculated by

$$U_{inine} = -\frac{i}{\lambda\sqrt{B^x_{p2d}B^y_{p2d}}}\int_{\mathbb{R}^2} G_1(u,v)(1-T(u,v)) \cdot\exp\left[i\frac{\pi}{\lambda B^x_{p2d}}\left(A^x_{p2d}u^2 - 2xu + D^x_{p2d}x^2\right)\right] \cdot\exp\left[i\frac{\pi}{\lambda B^y_{p2d}}\left(A^y_{p2d}v^2 - 2yv + D^v_{p2d}y^2\right)\right]\mathrm{d}u\mathrm{d}v, \tag{2}$$

where $T(x,y)$ denotes the particle in pipe. Note that the particle is considered as a hard aperture disk, and can be expressed as a complex Gaussian expansion $T(x,y) = \sum_{k=1}^{10} A_k \exp\left[-B_k\left(x^2+y^2\right)/r^2\right]$ [31]. The integral Eq. (2) has analytical solution [26]. U_{inline} is composed of the diffracted light of the particle in pipe $\mathbf{O}$, and the reference light $\mathbf{R}_p$ that passing through the pipe propagate and interfere with each other at the hologram plane (x,y), and the intensity of the optical field (regarded as inline hologram) can be written as

$$I_{inline} = U_{inline} * U^*_{inline} = \left[\mathbf{R}_p + \mathbf{O}\right]\cdot\left[\mathbf{R}^*_p + \mathbf{O}^*\right] = \mathbf{R}_p\cdot\mathbf{R}^*_p + \mathbf{O}\cdot\mathbf{O}^* + \mathbf{O}\cdot\mathbf{R}^*_p + \mathbf{R}_p\cdot\mathbf{O}^*, \tag{3}$$

the detailed expressions of the $\mathbf{R}_p$ and $\mathbf{O}$ can be found in Wu et al. [21]. The expressions in Eqs. (2) and (3) are well known formulas of optical field for typical digital inline holography that passing through lens

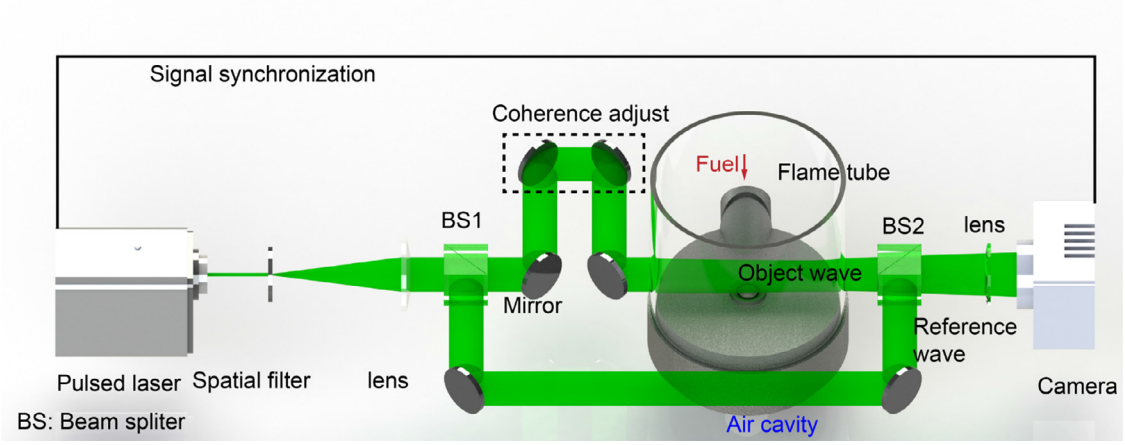

Fig. 1. Experimental setup of off-axis Fraunhofer holography viewing droplets inside the flame tube.

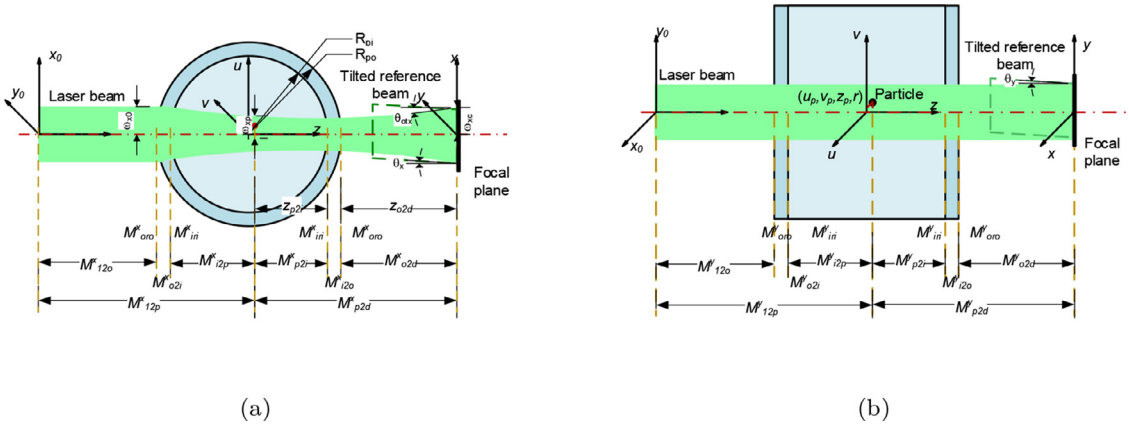

Fig. 2. Schematics laser propagation process of off-axis holography passing through a pipe. (a) Top view. (b) Front view.

system or a curved container and under the assumption of Fresnel approximation. The analysis of off-axis interference pattern will be carried out based on aforementioned results.

Denote the external plane wave tilted reference light as $\mathbf{R}_t = A_t \exp\left[-ikxsin(\theta_x) - iksin(\theta_y)\right]$, where A_t is the intensity of the tilted reference light. The off-axis hologram can be written as

$$\begin{aligned} I_H &= (\mathbf{R}_p + \mathbf{R}_t + \mathbf{O}) \cdot \left(\mathbf{R}_p^* + \mathbf{R}_t^* + \mathbf{O}^*\right) \\ &= \underbrace{\mathbf{R}_p \cdot \mathbf{R}_p^* + \mathbf{O} \cdot \mathbf{O}^* + \mathbf{R}_t \cdot \mathbf{R}_t^*}_{\text{direct terms}} + \underbrace{\mathbf{O} \cdot \mathbf{R}_p^* + \mathbf{R}_p \cdot \mathbf{O}^*}_{\text{inline holographic terms}} \\ &\quad + \underbrace{(\mathbf{O} + \mathbf{R}_p) \cdot \mathbf{R}_t^* + \left(\mathbf{R}_p^* + \mathbf{O}^*\right) \cdot \mathbf{R}_t}_{\text{off-axis holographic terms}}, \end{aligned} \tag{4}$$

in the expression, the first three terms are the direct terms, the fourth and fifth terms can be treated as the information of a digital inline hologram through a pipe, the sixth, seventh and the eighth, ninth are the $+1$ terms and conjugated terms separately, which contain the spatially modulated information of the object and the reference wave and the corresponding conjugated information separately. The interference pattern of the off-axis hologram can be inferred. Besides the inline holographic term, $\left(\mathbf{R}_p^* \cdot \mathbf{R}_t + \mathbf{R}_p \cdot \mathbf{R}_t^*\right)$ determines the off-axis fringes pattern. The complex amplitude distribution in the focus plane of $\mathbf{R}_p$ after analytical developments is

$$\mathbf{R}_p = \exp\left[-\left(\frac{x^2}{\omega_{xc}^2} + \frac{y^2}{\omega_{yc}^2}\right)\right] \exp\left[-i\frac{\pi}{\lambda}\left(\frac{x^2}{R_{xc}^2} + \frac{y^2}{R_{yc}^2}\right)\right], \tag{5}$$

where the $\omega_{xc,yc}$ are the beam radius and $R_{xc,yc}$ represent the wavefront curvature in the focal plane and have mathematical expressions as Verrier et al. [26]

$$\begin{aligned} \omega_{xc,yc} &= \left(\frac{\lambda B_{12d}^{x,y}}{\pi\omega_{x0,y0}}\right)\left[1 + \left(A_{12d}^{x,y} P_{12d}^{x,y}\right)^2\right]^{1/2}, \\ R_{xc,yc} &= -\frac{B_{12d}^{x,y}}{D_{12d}^{x,y} - \frac{A_{12d}^{x,y}\left(P_{12d}^{x,y}\right)^2}{1+\left(A_{12d}^{x,y} P_{12d}^{x,y}\right)^2}}, \quad \text{with} \quad P_{12d}^{x,y} = \frac{\pi\omega_{x0,y0}^2}{\lambda B_{12d}^{x,y}}, \end{aligned} \tag{6}$$

where the matrix elements $A_{12d}^{x,y}$, $B_{12d}^{x,y}$, and $D_{12d}^{x,y}$ are calculated from laser to focal plane and are determined by the system setup. Since the curvature of the straight pipe along y direction is infinite, $A_{12d}^{y} = D_{12d}^{y} = 1$, while P_{12d}^{y} is found to be much larger than 1, and thus R_{yc}^2 is much larger than the position y, indicating that $\left(\mathbf{R}_p^* \cdot \mathbf{R}_t\right)$ can be expressed as

$$\mathbf{R}_p^* \cdot \mathbf{R}_t = A_R(x,y) \exp\left\{-ik\left[\frac{(x+c_1)^2}{R_{xc}^2} + ysin(\theta_y) + \phi\right]\right\}, \tag{7}$$

where A_R represents the amplitude distribution, $c_1 = 0.5\sin(\theta_x)/R_{xc}^2$, and ϕ is the additional phase independent of the position. Eq. (7) indicates that the phase distribution of the interference pattern along y direction is linear, and the slope mainly depends on the off-axis angle θ_y, while the phase distribution along x direction obeys parabolic distribution, and the symmetry axis position depends on the θ_x.

3.2. Reconstruction of off-axis holography through a pipe

The main complex amplitude information of term $[\mathbf{O}+\mathbf{R}_\mathrm{p}]\cdot\mathbf{R}_\mathrm{t}^*$ can be separated from the others terms in the frequency domain, denoted as U_f. A tilted reference wave in a computer, and the spatial modulation of the object wave can be eliminated. Considering that the chriplet frequency is not equal along x and y directions, the classical convolution method or Fourier transform algorithm should be rescaled to take the magnifications into account. Using a modified kernel function of the convolution method as follows:

$$g(x,y,u,v,z_\mathrm{r})=\frac{i\exp\left(-ik\sqrt{S_x^2(x-u)^2+S_y^2(y-v)^2+z_\mathrm{r}^2}\right)}{\lambda\sqrt{S_x^2(x-u)^2+S_y^2(y-v)^2+z_\mathrm{r}^2}}, \tag{8}$$

where $k=2\pi/\lambda$ is the wave number, and the scale parameters $S_x^2=z_\mathrm{r}\left(R_{xp}-A^x_{\mathrm{p2d}}\right)/\left(B^x_{\mathrm{p2d}}\right)^2$, $S_y^2=z_\mathrm{r}\left(R_{yp}-A^y_{\mathrm{p2d}}\right)/\left(B^y_{\mathrm{p2d}}\right)^2$ are related with the transfer matrix, $R_{xp,yp}$ are the wavefront curvature in the particle plane, and the detailed calculation can be found in our previous study [21]. z_r is the reconstructed depth position.

The optical field of object can be reconstructed using fast Fourier transform (FFT):

$$\begin{aligned}\Gamma(x,y;z_\mathrm{r}) &= U_\mathrm{f}\mathbf{R}_\mathrm{t}\mathbf{R}_\mathrm{p}^*\otimes g(x,y,u,v)\\ &\simeq \mathcal{F}^{-1}\left\{\mathcal{F}\left[\left(\mathbf{O}\mathbf{R}_\mathrm{p}^*+\mathbf{R}_\mathrm{p}\mathbf{R}_\mathrm{p}^*\right)\cdot\mathbf{R}_\mathrm{t}^*\mathbf{R}_\mathrm{t}\right]\cdot\mathcal{F}(g)\right\},\end{aligned} \tag{9}$$

where $\otimes$ denotes the convolution operation. In the expression, only the phase introduced by tilted reference wave is eliminated. In fact, $\mathbf{R}_\mathrm{t}^*\mathbf{R}_\mathrm{t}$ and $\mathbf{R}_\mathrm{p}\mathbf{R}_\mathrm{p}^*$ can be treated as extra real values, which have no effect on the phase distribution. If the intensity amplitude of the tilted reference wave and the pipe reference wave are treated as unit, the expression somewhat consistent with that of digital inline holography using modified convolution reconstruction process. And the main advantage is that the conjugated term is filtered during the aforementioned reconstruction process.

It should be noticed that the reconstructed optical field might be different from the actual object field since there exists transverse shift and magnification. The magnification can be evaluated from the beam waist radius ratio at the particle and CCD plane: $M_{(x,y)}=\omega_{(xc,yc)}/\omega_{(xp,yp)}$, and the transverse shift can be evaluated by the origin point position of the world coordinate system in the image. When the optical set-up and the cylindrical window parameters are known, it is able to obtain the transverse magnifications $M_{x,y}$ and modified reconstruction coefficients $S^2_{(x,y)}$ based on aforementioned theoretical analysis. And the relations between parameter values and depth positions can be obtained, as seen in Fig. 3. Since the reconstructed field of view does not change with the z_r based on the proposed method, the extended focus image (EFI) can be calculated based on the wavelet transform,

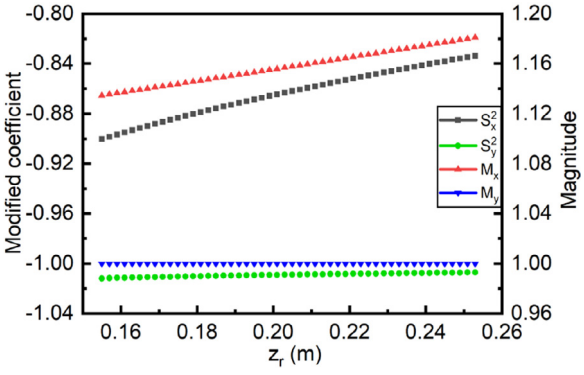

Fig. 3. Modified coefficients for the modified off-axis convolution method, and transverse magnification distribution, with pipe radius $R_\mathrm{pi}=53$ mm, $R_\mathrm{po}=56.75$ mm, refractive index $n_p=1.46$, and $z_{\mathrm{o2d}}=145$ mm.

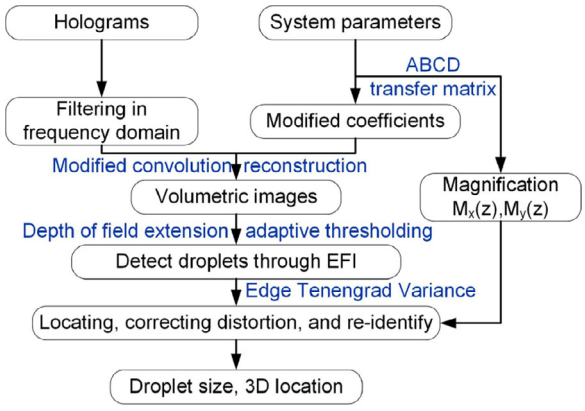

Fig. 4. Data processing procedure of particles in a circular flame tube with digital off-axis holography.

and the depth position can be first obtained using method introduced in Yingchun et al. [32], and then the real size and x, y positions are calculated based on magnification coefficients, as is summarized in Fig. 4

4. Results and discussions

4.1. Simulation analysis

Fig. 5(a) depicts the simulated off-axis hologram of an on-axis particle with diameter $d_p=500$ μm, and the object beam passes through the pipe, with $R_\mathrm{pi}=53$ mm, $R_\mathrm{po}=56.75$ mm, and the pipe refractive index $n_p=1.46$. The sub-figures in rectangular boxes depict three typical interference fringes of the off-axis hologram and corresponding digital inline hologram. The off-axis hologram has upwardly convex ($\theta_y>0$) or downwardly concave fringes ($\theta_y>0$), and when $\theta_y=0$, the off-axis fringes would be straight. and the local fringes are denser with distance from the optical axis along x direction. Fig. 5(b) compares the linear intensity distribution extracted from Fig. 5(a), and the intensity is normalized based on the initial incident beam. In addition to the interference fringes with the tiled reference beam, diffraction fringes containing object diameter and position information are also recorded. The chriplet signal of the particle does not change compared with the inline diffraction fringe, while the initial amplitude of the signal changes due to the influence of the off-axis interference fringes. The difference originates from the term $\left(\mathbf{O}\mathbf{R}_\mathrm{t}^*+\mathbf{O}^*\mathbf{R}_\mathrm{t}\right)$. Due to the curved surface of the pipe, the off-axis fringe frequency is linearly increased with distance from the central axis under the proposed theoretical model. As a consequence, the spatially modulated information appears as a bright line in the frequency domain, which corresponds to off-axis interference fringes that vary in density, as is shown in Fig. 5(c). The direct terms constitute the background intensity of the hologram, and appear as a bright spot in the centre of the frequency domain. The spot energy is relatively low since the energy of the object beam and reference beam are almost concentrated in the spatially modulated term. From Fig. 5(c), the local frequency f_y is a constant, while the $f_x=\sin(\theta_{otx})Nd_{pix}/\lambda$ is different along the x direction due to the concave geometry of the pipe, where N is the image pixel number along the x direction. The angle θ_{otx} changes with the x, since the collimated beam diverges in that direction along the z axis after passing through the pipe and he tilted reference light is collimated.

Thanks to off-axis setup, $\left(\mathbf{O}+\mathbf{R}_\mathrm{p}\right)\cdot\mathbf{R}_\mathrm{t}^*$ is able to be separated from the frequency domain, which is more convenient for further phase analysis compared with inline hologram. Fig. 5(d) depicts the wrapped phase distribution of the $\left(\mathbf{O}+\mathbf{R}_\mathrm{p}\right)$ based on simulation, which can be calculated by

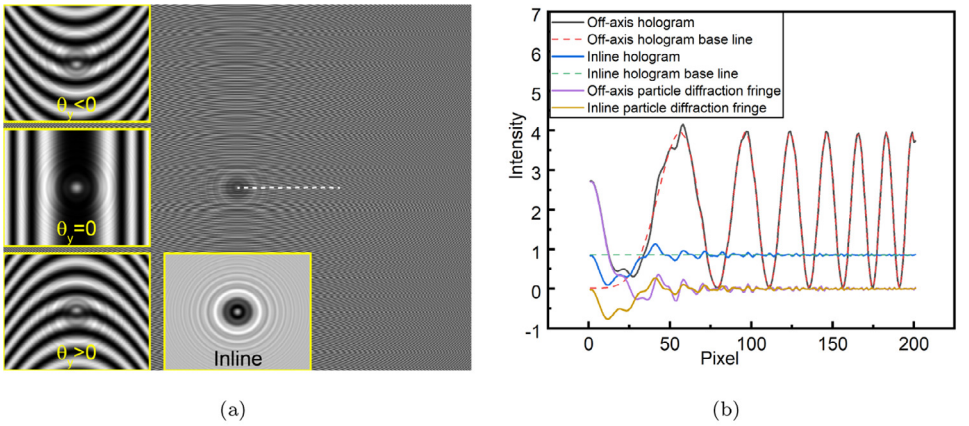

Fig. 5. Simulations of off-axis hologram passing through a pipe, with the tilted reference wave angle $\theta_x = 0$ rad. (a) Off-axis hologram, $\lambda = 532$ nm, $R_{pi} = 53$ mm, $R_{po} = 56.75$ mm, $n_p = 1.46$, $z_{p2i} = 53$ mm, $z_{o2d} = 145$ mm, $d_p = 500$ μ $\theta_y = 0.01$ rad. The subfigures shows different off-axis fringes of different θ_y in the yellow box, and the digital inline fringes for comparison. (b) Comparison of linear intensities extracted from off-axis hologram and inline hologram. (c) Frequency spectrum of hologram shown in Fig. 5(a), and the image contrast is enhanced. (d) Wrapped phase distribution of the object wave passing through a pipe. (For interpretation of the references to color in this figure legend, the reader is referred to the web version of this article.)

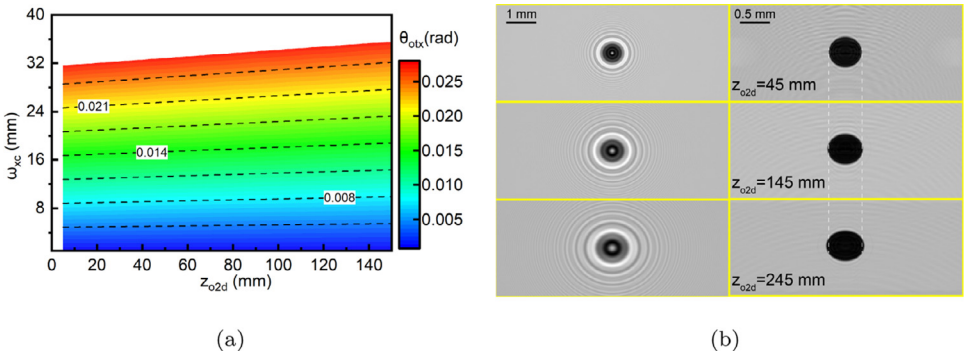

Fig. 6. (a) Tilted off-axis angle θ_{otx} of the object wave and the distribution with z_{o2d} and ω_{xc}. (b) Comparison of recorded inline fringes $\left(\mathbf{OR}_p^* + \mathbf{O}^*\mathbf{R}_p\right)$ and reconstructed particle images from off-axis holograms at different z_{o2d}.

$(\varphi)_{w1} = \arctan\left\{\mathrm{Re}\left[(\mathbf{O}+\mathbf{R}_p)\cdot\mathbf{R}_t^*\mathbf{R}_t\right]/\mathrm{Im}\left[(\mathbf{O}+\mathbf{R}_p)\cdot\mathbf{R}_t^*\mathbf{R}_t\right]\right\}$. $(\varphi)_{w1}$ contains both the wrapped phase brought by the pipe and the phase from particle signal. If the conjugated reference wave $\mathbf{R}_p^*$ is introduced during reconstruction process, the phase caused by the pipe can be compensated. The phase of the reconstructed result can be obtained from $(\varphi)_{w2} = \arctan\left\{\mathrm{Re}\left[(\mathbf{O}+\mathbf{R}_p)\cdot\mathbf{R}_t^*\mathbf{R}_t\mathbf{R}_p^*\right]/\mathrm{Im}\left[(\mathbf{O}+\mathbf{R}_p)\cdot\mathbf{R}_t^*\mathbf{R}_t\mathbf{R}_p^*\right]\right\}$, which just contains the wrapped phase from particle signal. In the expression, $\mathbf{R}_t^*\mathbf{R}_t$ and $\mathbf{R}_p\mathbf{R}_p^*$ do not change phase distribution.

For off-axis hologram, the Nyquist sampling law should be satisfied during recording, and thus the local off-axis angle between the object wave and the reference wave θ_{otr} should be limited. Based on the ABCD matrix, the function of θ_{otx} with x and z can be calculated, and the results of aforementioned experimental system is shown in Fig. 6(a). It can be found that θ_{otx} is linear related to ω_{xc} based on matrices calculation. Note that the Nyquist's sampling law should be satisfied during recording, the $\theta_{otry} = \theta_y$, and the $\theta_{otrx} = \theta_{otx} + \theta_x \le \lambda/2d_{\mathrm{pix}}$. θ_x would shift the bright line in frequency spectrum horizontally, making it harder for the recorded system to satisfy Nyquist's sampling law. As a consequence, it is better to set the θ_x to be zero, and the spatial modulation can be achieved by setting appropriate θ_y. It can also be inferred from the figure that the magnification of the same particle in the tube varies with different z_{o2d}, the figure shows three focused particle images at three $z_{o2d} = 45$ mm, 145 mm and 245 mm, and the magnification $M_x = 1.081$, 1.171, and 1.264 separately.

The depth positions of particles in the pipe correspond to different modified coefficients, and the particles with different depth positions have different aberrations. Fig. 7 shows three reconstructed

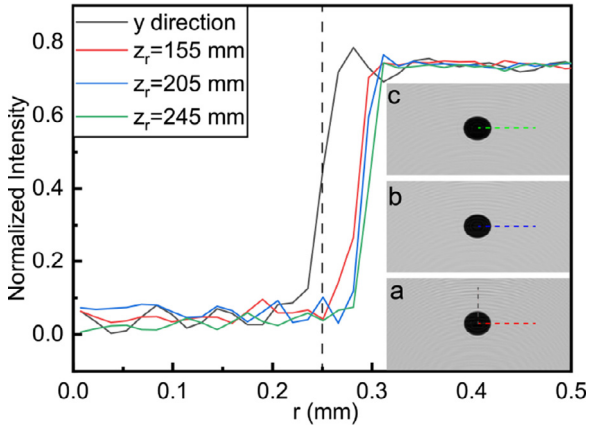

Fig. 7. Focused droplet images and intensity distributions of focus particles at different depth positions, with z_{o2d} = 145 mm. a, droplet at z_r = 155 mm, M_x = 1.151. b, droplet at z_r = 205 mm, M_x = 1.168. c, droplet at z_r = 245 mm, M_x = 1.195.

focused particle images based on simulated holograms with on-axis particle diameter of 500 μm in different depth positions, and their corresponding normalized intensity distributions along x and y directions. The particle focused well in both x and y direction, revealing that the astigmatism caused by the pipe has been eliminated. Still, the distortion exists. Imaging result shows that vertical direction of the particle is not stretched, while the horizontal distortion needs to be corrected. Note that the focused particle position (x_r, y_r, z_r) is the established based on hologram coordinate system, and the (x_r, y_r) has the same scale with image on camera target, z_r is the distance between particle and camera target. The true coordinate (x_p, y_p, z_p) can be determined based on the magnification value on z_r, and $z_p = z_r$.

4.2. Experimental validation

Fig. 8 shows the treating results of an experimental hologram of a standard glass plane calibrator in pipe. The tilted reference wave was modulated to let $\theta_x = 0$ rad, and θ_y has a certain value of about 0.0093 rad. Downwardly convex interference fringes can be observed in Fig. 8(a). Two bright lines corresponding to the off-axis holographic terms are shown in Fig. 8(b), and a bright centre can also be observed in the frequency spectrum, which corresponds to the direct terms and inline holographic terms. The phase pattern of the object wave in experiment shown in Fig. 8(c) also characterizes the additional phase caused by the pipe and other optical elements. Fig. 8(d) depicts the unwrapped phase from purely simulated off-axis hologram and background off-axis hologram obtained in the experiment. The phase distribution of the experimental result also follows the parabolic distribution, and the average phase deviation between experiment and the parabolic fit is about 4.8 rad, revealing that the theoretical analysis is basically consistent with the experiment in the case of paraxial approximation. The deviation between the experimental phase and the parabolic fit is mainly due to the machining error of the pipe and the optical system.

Fig. 9 (a) depicts a clear reconstruction image of calibrator without astigmatism with magnification M_x =1.151, and Fig. 9(b) shows the distortion eliminated image based on the proposed model. The size error, x, and y locating error can be evaluated since the relative positions of the standard dots are known, and the calibrating results can be seen in Fig. 9(c). Here, the reconstructed slice is corrected firstly,

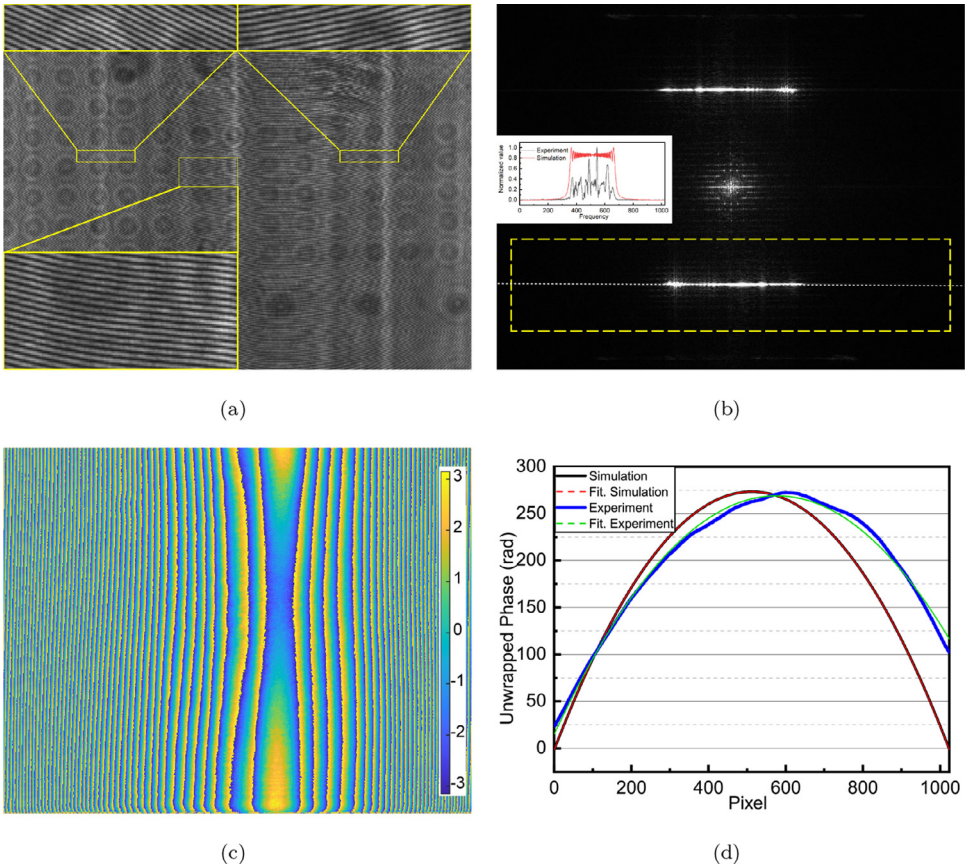

Fig. 8. Data treating results of an experimental hologram of a standard calibrator. (a) Hologram. (b) Frequency spectrum of the hologram shown in Fig. 8(a). (c) Wrapped phase distribution of background off-axis experimental hologram. (d) Corresponding unwrapped phase distribution of experimental hologram shown in Fig. 8(c) and simulated hologram shown in Fig. 5(a).

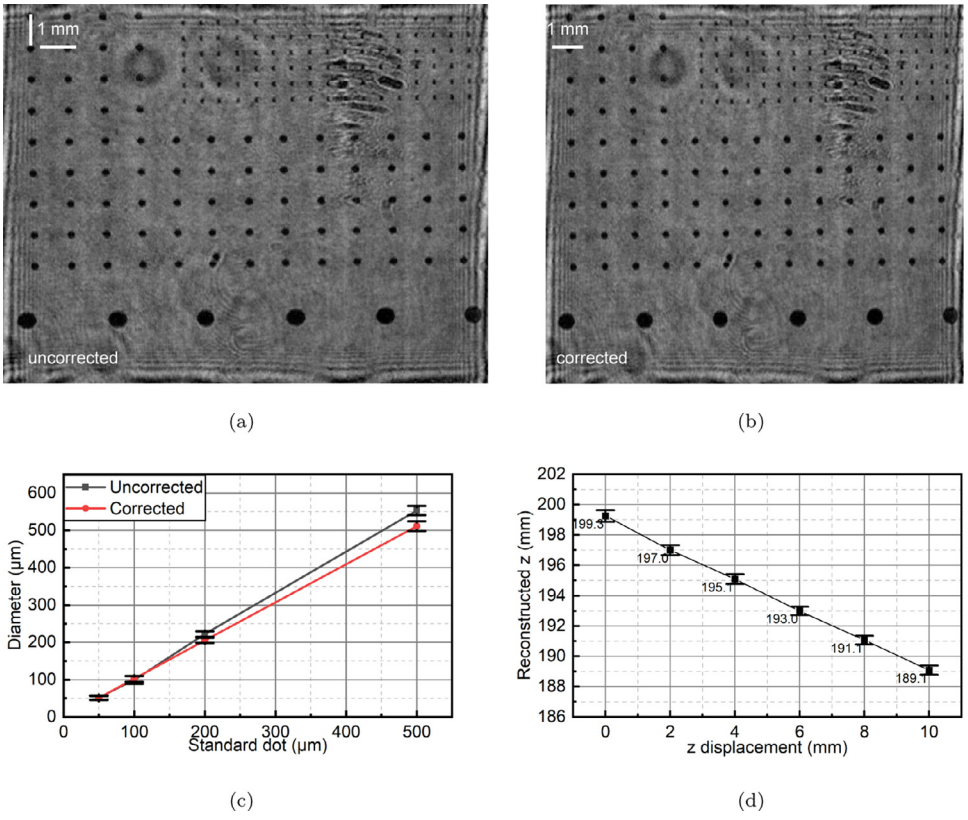

Fig. 9. Reconstructed image, size measurement error and z locating error through calibration. (a) Reconstructed focused particle image at $z_r = 201$ mm, with $S_x^2 = -0.8590$, $S_y^2 = -1.0098$, and magnification $M_x = 1.151$. (b) The corrected focus image; (c) Size; (d) z location calibration.

and then particles are detected, and the sizes are defined by the diameter of the circle that have the same cross-section areas. The average measured size and relative error are depicted in Fig. 9(c). The average calibration of standard dot with sizes of 50 μm, 100 μm, 200 μm and 500 μm are 51 μm, 102 μm, 204 μm, and 510 μm respectively, with standard deviation under 13 μm, and the average x and y position error is also calculated to be lower than one equivalent pixel width. The z locating error is also evaluated through displacing standard calibrator to different depth positions, as shown in Fig. 9(d). The data points represent the average z position of the standard dots in one calibrator, and the error bars represent the standard deviation of z. The reconstructed z offset is basically the consistence with the calibration displacement, with average deviation about 300 μm/10 mm. The average z repeating locating error of a single standard dot is under 0.4 mm, but the standard deviation of dot in calibrator is under 1.5 mm probably due to the discrepancy of the local curvature of the pipe and the existence of the background noise. The precise locating of z is expected to be obtained by means of tomographic holography [33] based on this study. In general, although the existence of the pipe indeed affects the test accuracy, and there exists difference between the actual pipe and the theoretical assumption. The proposed model is still effective in mitigating the astigmatism and distortion aberration of the reconstructed image, and eliminating the conjugated term which may influence the imaging quality.

As a practical attempt at this technology, Fig. 10 presents the experimental results of a swirl combustion spray field in the near nozzle region inside the silicon pipe, and the direct imaging of flame can be seen in Fig. 1. Fig. 10(a) is the off-axis hologram of the combustion field, and the overall interference fringes are downwardly concave due to the effect of the pipe window, besides, the inhomogeneous refractive index gradient of the turbulent combustion field also changes the local frequency of the interference fringes and caused the optical ripple, as refereed in Fig. 10(a). Despite the aforementioned disturbance, clear visualization of the fuel droplets near the swirler exist can be presented with the proposed method, as shown in Fig. 10(b), and the EFI is obtained based on wavelet image fusion algorithm [32]. Since the proposed method focuses particles in both x and y directions at the same depth position. The FMC of discrete droplet calculated based on the particle edge variance had an obvious single front, in which the location of the peak corresponds to the depth position, as depicted in Fig. 10(c). Droplet size and 3D location are also quantified after the distortion correction process. Fig. 10(d) shows typical droplets transportation trajectories obtained from the time-resolved holograms, in which particle 3D position and size are corrected. It can be found that the projected traces in $x - y$ plane are smooth, which proves the feasibility of this study. It should be noticed that there exist strong refractive index gradient in the turbulent flame, and the locating error of the depth may be larger and even reach to over hundreds of micrometers due to the unknown refractive index distribution, and the traces along z direction are not smooth. Accurate z locating can be achieved by technical means such as tomography [33–35]. It is also worth noting that the proposed method is derived base on axial approximation assumption, which means that when the off-axis angle of the object wave is too large, the assumption is not feasible and the proposed method would face a larger measurement error. In this study, the swirler locates in the middle of the circular flame tube, with a diameter of 20 mm, and the off-axis angle θ_{otrx} satisfies the assumptions as well as the Nyquist sampling theory. Nevertheless, the method proposed in this study still proved its feasibility in particle visualization and quantification in a complex environment through a concave pipe, and the droplet size, x and y position are able to be quantified accurately through calibration and distortion correction.

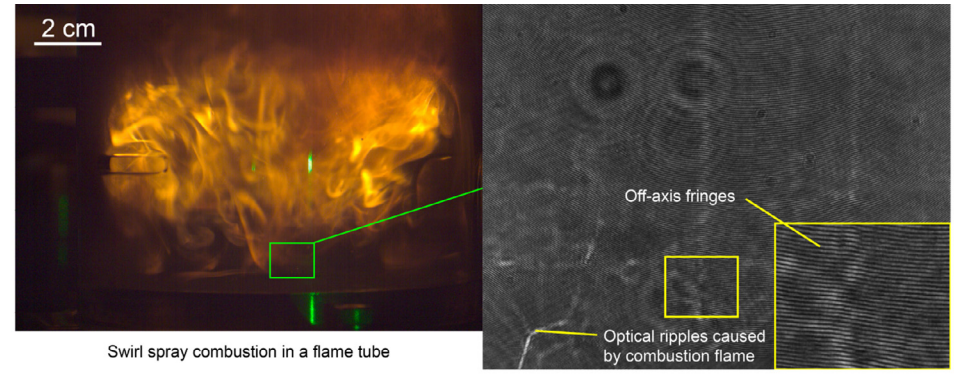

(a)

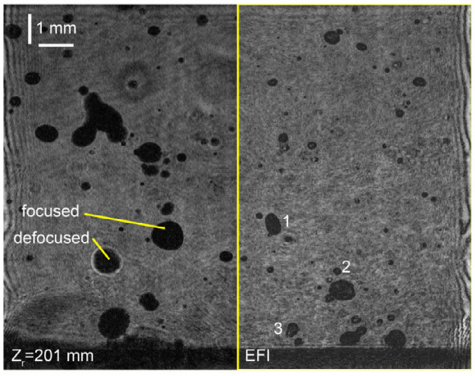

(b)

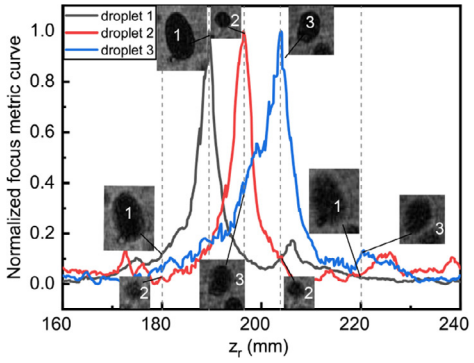

(c)

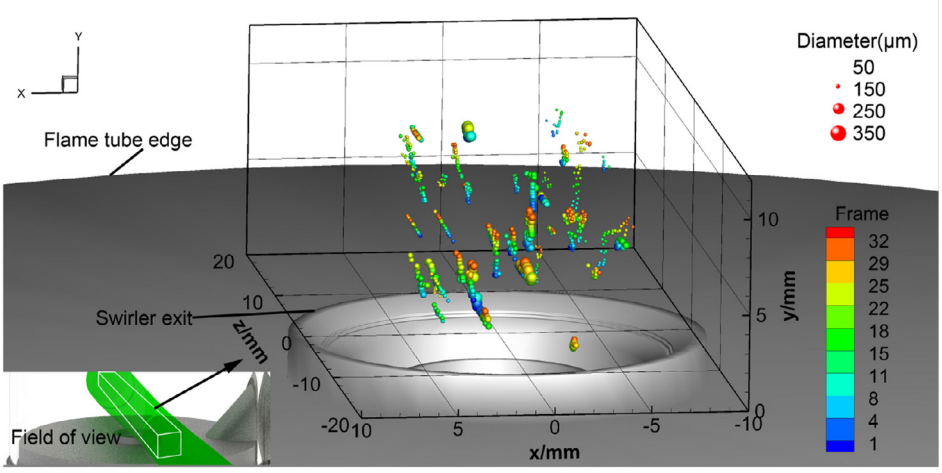

(d)

Fig. 10. Fuel droplet visualization of typical turbulent spray combustion field in a pipe chamber. (a) Direct imaging of a swirl spray combustion field in a flame tube, and corresponding hologram, with fuel flow rate of 0.3 g/s, and gas pressure of 0.5 kPa. (b) Reconstructed slice and extended focus image(EFI) of the hologram, $z_r = 201$ mm.(c) FMCs of droplets shown in (b). (d) Typical 3D trajectories of the droplets obtained from 32 consecutive holograms after distortion correction process.

5. Conclusion

Facing the actual requirements of the multiphase flow test in a curved container like the flame tube, in this study, the theoretical analysis and verification of astigmatic digital off-axis holography for particle measurement in a circular flame tube are proposed and discussed. The conclusions are as follows:

- A theoretical model for digital off-axis hologram passing through a pipe is established. Three different types of interference fringes are simulated and the additional phase introduced by the pipe is discussed, and the results are consistent with the theoretical analysis based on the integral formula.
- A modified convolutional reconstruction method facing off-axis holography is proposed. The simulation reconstruction results reveal that the proposed method can eliminate the conjugated term and obtain a clear particle image without astigmatism, yet the geometric aberration exists and needs to be corrected based on the ABCD transfer matrix.
- The proposed theoretical method and reconstruction algorithm is validated by experimental calibration. The additional unwrapped phase caused by pipe also follows parabolic distribution basically, revealing the feasibility of the theoretical analysis. Particle size and z locating error are obtained using a standard dot calibrator. The average size deviation, and x, y position error is lower than one-pixel

width. The average repeating z locating error of a single calibrator dot is within 0.4 mm, while the average z locating deviation of different standard dots in the field of view is within 1.5 mm due to the manufacturing error of the pipe in the experiment. The overall z displacement of the calibrators can be restored by the proposed algorithm, with the error of about 300 μm/10 mm.

- The proposed method is applied to the burning fuel droplets measurement in a flame tube in swirl turbulent combustion field. Clear fuel droplet morphology, as well as droplet size, 3D position and trajectory can be visualized and quantified. The z position error makes the 3D trajectory oscillate. More precise depth position depends on advanced techniques like tomo-holography.

In conclusion, the proposed technology and corresponding data processing method provide an effective and powerful way to visualize and quantify the multiphase flow in a curve container. The application proves the feasibility of viewing particles in a complex environment. The proposed method is valid when both the paraxial approximation assumption and Nyquist's sampling law are satisfied.

Declaration of Competing Interest

The authors declare that they have no known competing financial interests or personal relationships that could have appeared to influence the work reported in this paper.

CRediT authorship contribution statement

Lei Wang: Conceptualization, Writing – original draft, Software, Writing – review & editing, Data curation, Methodology, Investigation. **Yue Zhao:** Investigation, Visualization, Writing – review & editing. **Yu Wang:** Data curation, Investigation. **Yingchun Wu:** Conceptualization, Supervision, Software, Methodology, Funding acquisition. **Ge Song:** Resources, Supervision. **Tao Liu:** Resources, Supervision. **Xuecheng Wu:** Resources, Project administration, Funding acquisition.

Data availability

Data will be made available on request.

Acknowledgment

The authors gratefully acknowledge the support from National Science and Technology Major Project (J2019-III-0006-0049).

Appendix A

The ABCD matrix from the beam waist plane to the particle plane can be expressed as

$$\mathbf{M}_{\mathrm{l2p}}^{x,y}=\mathbf{M}_{\mathrm{i2p}}^{x,y}\mathbf{M}_{\mathrm{iri}}^{x,y}\mathbf{M}_{\mathrm{o2i}}^{x,y}\mathbf{M}_{\mathrm{ori}}^{x,y}\mathbf{M}_{l2o}^{x,y}=\begin{bmatrix}A_{\mathrm{l2p}}^{x,y} & B_{\mathrm{l2p}}^{x,y}\\ C_{\mathrm{l2p}}^{x,y} & D_{\mathrm{l2p}}^{x,y}\end{bmatrix}, \tag{10}$$

where $\mathbf{M}_{\mathrm{l2o}}^{x,y}$ represents the free space propagation form the beam waist plane to the outer surface of the pipe, $\mathbf{M}_{\mathrm{ori}}^{x,y}$ means the refraction at the outer surface of the pipe, $\mathbf{M}_{\mathrm{o2i}}^{x,y}$ represents the beam propagates form the outer surface to the inner surface of the pipe, $\mathbf{M}_{\mathrm{iri}}^{x,y}$ means the refraction at the inner surface of the pipe, and $\mathbf{M}_{\mathrm{i2p}}^{x,y}$ represents the beam propagates from the inner surface to the object. The details of the matrix expression can be found in Wu et al. [22], Gerrard and Burch [36].

The ABCD matrix from the particle plane to the camera target can be expressed as

$$\mathbf{M}_{\mathrm{p2d}}^{x,y}=\mathbf{M}_{\mathrm{o2d}}^{x,y}\mathbf{M}_{\mathrm{oro}}^{x,y}\mathbf{M}_{\mathrm{i2o}}^{x,y}\mathbf{M}_{\mathrm{iro}}^{x,y}\mathbf{M}_{\mathrm{p2i}}^{x,y}=\begin{bmatrix}A_{\mathrm{p2d}}^{x,y} & B_{\mathrm{p2d}}^{x,y}\\ C_{\mathrm{p2d}}^{x,y} & D_{\mathrm{p2d}}^{x,y}\end{bmatrix}, \tag{11}$$

where $\mathbf{M}_{\mathrm{p2d}}^{x,y}$ characterizes the optical system of the particle to the recording plane, $\mathbf{M}_{\mathrm{o2d}}^{x,y}$ means the propagation from the out surface to the recording plane, $\mathbf{M}_{\mathrm{oro}}^{x,y}$ represents the refraction at the outer surface of the pipe, $\mathbf{M}_{\mathrm{i2o}}^{x,y}$ means the beam propagates from the inner surface to the outer surface of the pipe. $\mathbf{M}_{\mathrm{iri}}^{x,y}$ means the refraction at the inner surface of the pipe, and $\mathbf{M}_{\mathrm{p2i}}^{x,y}$ represents the beam propagates from the particle to the inner surface to the object. The details of the matrix expression can also be found in Wu et al. [22], Gerrard and Burch [36].

Supplementary material

Supplementary material associated with this article can be found, in the online version, at 10.1016/j.optlaseng.2022.107219

References

[1] Lamadie F, Sentis M, Bruel L. Digital in-line holography for near field observation of liquid-liquid flows under astigmatic conditions. In: The 11th international conference on laser-light and interactions with particles; 2016.
[2] Boxx I, Slabaugh C, Kutne P, Lucht RP, Meier W. 3 kHz PIV/OH-PLIF measurements in a gas turbine combustor at elevated pressure. Proc Combust Inst 2015;35(3):3793–802.
[3] Salaün E, Malbois P, Vandel A, Godard G, Grisch F, Renou B, Cabot G, Boukhalfa A. Experimental investigation of a spray swirled flame in gas turbine model combustor. In: 18th international symposium on the application of laser and imaging techniques to fluid mechanics, Lisbon, Portugal; 2016. p. 9.
[4] Petersen B, Miles P. Piv measurements in the swirl-plane of a motored light-duty diesel engine. SAE Int J Engines 2011;4(1):1623–41.
[5] Lee SJ, Byeon HJ, Seo KW. Inertial migration of spherical elastic phytoplankton in pipe flow. Exp Fluids 2014;55(6):1742.
[6] Zhou Z, S SK, Mallery K, Jiang W, Hong J. Holographic astigmatic particle tracking velocimetry (HAPTV). Meas Sci Technol 2020;31(6):065202.
[7] Parker J, Merati P. An investigation of turbulent Taylor–Couette flow using laser Doppler velocimetry in a refractive index matched facility. J Fluids Eng 1996;118(4):810–18.
[8] Kim S, Lee SJ. Measurement of 3D laminar flow inside a micro tube using micro digital holographic particle tracking velocimetry. J Micromech Microeng 2007;17(10):2157.
[9] Huisman SG, van Gils DPM, Sun C. Applying laser Doppler anemometry inside a Taylor–Couette geometry using a ray-tracer to correct for curvature effects. Eur J Mech - B/Fluids 2012;36:115–19.
[10] Stansfield P, Wigley G, Justham T, Catto J, Pitcher G. PIV analysis of in-cylinder flow structures over a range of realistic engine speeds. Exp Fluids 2007;43(1):135–46.
[11] Schnars U., Falldorf C., Watson J., Jüptner W.. Digital holography digital holography and wavefront sensing. 2015.
[12] Coetmellec Sebastien, Verrier Nicolas, Brunel M, Lebrun Denis. General formulation of digital in-line holography from correlation with a chirplet function. J Eur Opt Soc Rapid Publ 2010;5:10027. doi:10.2971/jeos.2010.10027.
[13] Coetmellec S, Wichitwong W, Gréhan G, Lebrun D, Brunel M, Janssen AJEM. Digital in-line holography assessment for general phase and opaque particle. J Eur Opt Soc Rapid Publ 2014;9:14021. https://www.jeos.org/index.php/jeos_rp/article/view/14021.
[14] Huang J, Cai W, Wu Y, Wu X. Recent advances and applications of digital holography in multiphase reactive/nonreactive flows: a review. Meas Sci Technol 2021;33(2):022001.
[15] Collins SA. Lens-system diffraction integral written in terms of matrix optics. JOSA 1970;60(9):1168–77.
[16] Bernardo Luis. ABCD matrix formalism of fractional Fourier optics. J Opt Eng 1996;35(3):732–40. doi:10.1117/1.600641.
[17] Sentis MPL, Bruel L, Charton S, Onofri FRA, Lamadie F. Digital in-line holography for the characterization of flowing particles in astigmatic optical systems. Opt Lasers Eng 2017;88:184–96.
[18] Coëtmellec S, Lebrun D, Ozkul C. Characterization of diffraction patterns directly from in-line holograms with the fractional Fourier transform. Appl Opt 2002;41(2):312–19.
[19] Verrier N, Coëtmellec S, Brunel M, Lebrun D, Janssen AJEM. Digital in-line holography with an elliptical, astigmatic Gaussian beam: wide-angle reconstruction. J Opt Soc Am A 2008;25(6):1459–66.
[20] Nicolas F, Coëtmellec S, Brunel M, Allano D, Lebrun D, Janssen AJEM. Application of the fractional Fourier transformation to digital holography recorded by an elliptical, astigmatic Gaussian beam. J Opt Soc Am A 2005;22(11):2569–77.
[21] Wu X, Wu Y, Yang J, Wang Z, Zhou B, Gréhan G, et al. Modified convolution method to reconstruct particle hologram with an elliptical Gaussian beam illumination. Opt Express 2013;21(10):12803–14.
[22] Wu Y, Wu X, Yao L, Gréhan G, Cen K. Direct measurement of particle size and 3D velocity of a gas solid pipe flow with digital holographic particle tracking velocimetry. Appl Opt 2015;54(9):2514–23.
[23] Lin W-K, Matoba O, Lin B-S, Su W-C. Astigmatism correction and quality optimization of computer-generated holograms for holographic waveguide displays. Opt Express 2020;28(4):5519–27.
[24] Remacha C, Coëtmellec S, Brunel M, Lebrun D. Extended wavelet transformation to digital holographic reconstruction: application to the elliptical, astigmatic Gaussian beams. Appl Opt 2013;52(4):838–48.
[25] Palma C, Bagini V. Extension of the fresnel transform to ABCD systems. J Opt Soc Am A 1997;14(8):1774–9.

[26] Verrier N, Coëtmellec S, Brunel M, Lebrun D. Digital in-line holography in thick optical systems: application to visualization in pipes. Appl Opt 2008;47(22):4147–57.
[27] Verrier N, Remacha C, Brunel M, Lebrun D, Coëtmellec S. Micropipe flow visualization using digital in-line holographic microscopy. Opt Express 2010;18(8):7807–19.
[28] Trolinger JD, Heap MP. Coal particle combustion studied by holography. Appl Opt 1979;18(11):1757–62.
[29] Yao L, Yu L, Lin X, Wu Y, Chen J, Zheng C, et al. High-speed digital off-axis holography to study atomization and evaporation of burning droplets. Combust Flame 2021;230:111443.
[30] Wu Y, Wang L, Lin W, Song G, He Y, Wu X, et al. Picosecond pulsed digital off-axis holography for near-nozzle droplet size and 3D distribution measurement of a swirl kerosene spray. Fuel 2021;283:119124.
[31] Wen JJ, Breazeale MA. A diffraction beam field expressed as the superposition of Gaussian beams. J Acoust Soc Am 1988;83(5):1752–6.
[32] Yingchun W, Xuecheng W, Jing Y, Zhihua W, Xiang G, Binwu Z, et al. Wavelet-based depth-of-field extension, accurate autofocusing, and particle pairing for digital inline particle holography. Appl Opt 2014;53(4):556–64.
[33] Soria J, Atkinson C. Towards 3C-3D digital holographic fluid velocity vector field measurement-tomographic digital holographic PIV (Tomo-HPIV). Meas Sci Technol 2008;19(7):074002.
[34] Gao J, Katz J. Self-calibrated microscopic dual-view tomographic holography for 3D flow measurements. Opt Express 2018;26(13):16708–25.
[35] Wu Y, Zhang H, Wu X, Cen K. Dual-view tomographic particle holography: modeling and light scattering effects. J Quant Spectrosc Radiat Transf 2020;255:107232.
[36] Gerrard A, Burch JM. Introduction to matrix methods in optics. Courier Corporation; 1994. ISBN 0486680444.